

Elevated foehn exacerbates surface ozone pollution in summer Beijing

Zhiheng Liao¹, Jing Xu¹, Ju Li¹, Liyan Zhou¹, Chao Liu¹, Lin Wu², Zhiqiang Ma¹

¹Institute of Urban Meteorology, China Meteorological Administration, Beijing, China;

²Huairou Meteorological Office of Beijing, Beijing, China.

Correspondence: Z. Liao (zh_liao@ium.cn) and Z. Ma (zqma@ium.cn)

Abstract: While several studies have evaluated the impact of shallow foehn on air pollution, the effects of elevated foehn on O₃ pollution remain poorly understood. Here, we investigate the role of elevated foehn in summer O₃ pollution in Beijing through detailed case analysis and a long-term climatological evaluation. The case study reveals that elevated foehn exacerbates next-day O₃ pollution through three primary mechanisms: first, by increasing boundary layer temperature, thereby enhancing photochemical O₃ formation; second, by reducing the residual/boundary layer height, thereby inhibiting vertical diffusion of pollutants; and third, by slowing boundary layer winds, thereby suppressing horizontal dispersion. A ten-year climatological evaluation of 54 identified elevated foehn events strongly supports these mechanisms. On average, these events led to a post-foehn afternoon boundary layer temperature increase exceeding 3°C, an afternoon boundary layer height reduction of more than 100 m, and a decrease in afternoon boundary layer wind speed of more than 1.0 m s⁻¹ compared to the pre-foehn days. Consequently, 87% of elevated foehn events were associated with a worsening of O₃ pollution. Post-foehn daily maximum 8-hour average O₃ concentrations frequently surpassed the national pollution threshold (160 µg m⁻³), with an average increase of 20%–60% (varying by site and higher in urban areas) compared to preceding days. These results demonstrate a robust and deterministic exacerbating effect of elevated foehn on surface O₃ pollution, suggesting that elevated foehn can serve as a reliable meteorological precursor for O₃ pollution warnings in summer Beijing.

Keywords: elevated foehn, atmospheric boundary layer, residual layer warming, ozone pollution, Beijing

1. Introduction

Foehn is a phenomenon of downslope winds with significant warming on the mountain leeward side (Elvidge and Renfrew, 2016). It has been observed among many large mountains in the world, including the Alpine Mountains (Miltenberger et al., 2016; Seibert et al., 2000), Rocky Mountains (Kerr, 1986), Appalachian Mountains (Gaffin, 2002, 2009), Taihang Mountains (Li et al., 2020a; Li et al., 2025), and Tianshan Mountains (Li et al., 2015; Li et al., 2020b). The societal and economic impacts of foehn winds are wide-ranging and well-documented, encompassing enhanced fire risks, extreme heat exposure, impacts on air quality, beneficial impacts on agriculture, and direct wind-driven damage to infrastructure. Given these multifaceted impacts, foehn has long been a subject of sustained scholarly interest across diverse disciplines.

Scientific research into the effect of foehn on air pollution began in Europe in the late nineteenth century, primarily to explain elevated ozone (O₃) levels in the Alpine regions during foehn events (Baumann et al., 2001; Campana et al., 2005; Seibert et al., 2000). Early European studies identified that the initial rise in O₃ concentration was caused by the advection of residual-layer air masses from source regions such as the Po Basin. Later on, O₃ levels in the foehn-affected area were found to be influenced by regional-scale advection from the lower free troposphere or even the stratosphere. Collectively, these studies emphasized the transport role of foehn in influencing O₃ air quality in the relatively clean valleys of Alps. In contrast, research in China has commonly demonstrated a “clearance

45 effect” of foehn on air pollution in highly-polluted cities (Li et al., 2020a; Li et al., 2025; Yang et al., 2018). For
46 example, Yang et al. (2018) reported a case in Shijiazhuang where foehn led to rapidly improved horizontal visibility,
47 decreased aerosol concentration, and weakened haze intensity. Similarly, a six-year statistical study by Li et al. (2025)
48 found that 60.4 % of foehn events were associated with a subsequent decrease in fine particulate matter (PM_{2.5})
49 concentrations in Beijing. This clearance effect is attributed to the origin of the foehn winds, which typically transport
50 cleaner air from the less polluted western, northwestern and northern mountain areas of the Hebei–Beijing region
51 into more polluted plains.

52
53 These abovementioned studies, conducted in both Europe and China, primarily examine the foehn effect on air
54 pollution mainly from a dynamical (transport) perspective. Furthermore, the foehn cases selected in these studies are
55 generally confined to shallow foehns, identifying using near-surface meteorological observations. Crucially, however,
56 the defining feature of foehn is the associated warming (Elvidge and Renfrew, 2016). This warming inevitably alters
57 the vertical thermal structure—and thus the atmospheric stability—which directly governs the capacity for vertical
58 diffusion of air pollutants (Liao et al., 2018; Stull, 1988). Therefore, the vertical extent of the foehn (shallow or
59 elevated) critically determines its impact on atmospheric stability: shallow foehn tends to enhance near-surface
60 instability, while elevated foehn can strengthen stability within or above the boundary layer. From this
61 thermodynamic perspective, elevated foehn likely possesses a greater pollution potential than its shallow counterpart.
62 Despite this reasoning, to the best of our knowledge, only one study—Li et al. (2015) in Urumqi, a city adjacent to
63 Tianshan Mountains—has explicitly investigated the impact of an elevated foehn on air pollution from a
64 thermodynamic viewpoint. That study revealed that an elevated southeasterly foehn layer between 480 and 2100 m
65 created a very stable boundary layer structure, which suppressed vertical mixing and led to severe haze pollution
66 episodes. Recent studies on PM_{2.5} pollution in Beijing (Li et al., 2020a; Li et al., 2025) have speculated that post-
67 foehn pollution exacerbation might be driven by a mechanism similar to the elevated foehn process observed in
68 Urumqi (Li et al., 2015). However, the existence and role of such an elevated foehn mechanism have not yet been
69 observationally confirmed for Beijing.

70
71 Beijing, the capital of China, faces significant challenges in terms of air pollution. Particularly in recent summers,
72 O₃ has surpassed PM_{2.5} as the most important air pollutant, arousing widespread attention (Liao et al., 2023; Zong et
73 al., 2023). The city’s location on the plains adjacent to the Taihang Mountains to the west and the Yan Mountains to
74 the north makes it particularly susceptible to foehn winds (Xu et al., 2026). Luo et al. (2020) documented an intensive
75 foehn warming event in Beijing where nocturnal air temperatures increased by over 10°C per hour. Utilizing data
76 from a density automatic weather station network, Li et al. (2025) developed a foehn identification method and
77 reported an annual average of 56.5 foehn days in Beijing. As noted earlier, their statistical analysis suggests a higher
78 probability of PM_{2.5} pollution alleviation (60.4 %) rather than pollution exacerbation (39.6 %) following foehn events
79 in Beijing. Importantly, because their identification method only relies on near-surface observations, the detected
80 events are predominantly shallow foehns. This methodological focus may obscure the distinct air pollution effects
81 potentially caused by elevated foehns. Therefore, determining whether elevated foehn induces a more deterministic—
82 and likely adverse—pollution effects is a critical unanswered question. The answer has practical importance, as it
83 would inform whether elevated foehn can serve as a reliable precursor indicator for air pollution warnings, thereby
84 improving mitigation efforts in Beijing and other leaside cities.

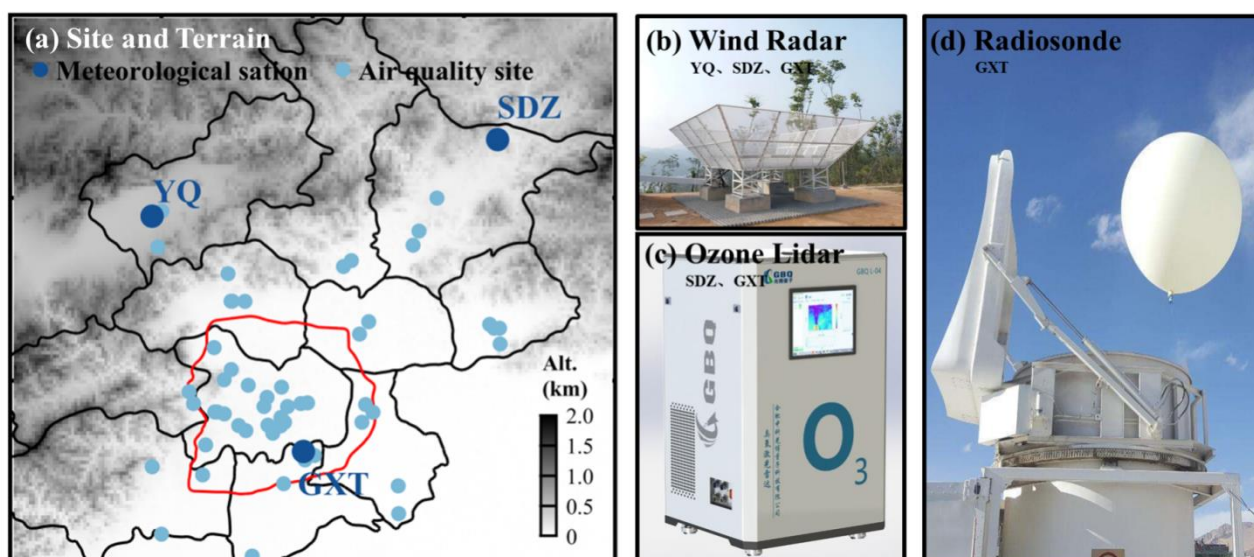
85
86 To address this knowledge gap, our team deployed two O₃ lidars at an urban (Guanxiangtai, GXT) and a rural
87 (Shangdianzi, SDZ) station in Beijing in late July 2024. This coordinated dual-station lidar setup is particularly suited
88 to capturing the three-dimensional characteristics and mechanisms of boundary layer O₃ evolution under the influence

89 of elevated foehn. One month after deployment (27–31 August), we observed an O₃ pollution episode associated with
90 an elevated foehn. In this study, we conducted a detailed analysis of this event by integrating data from the new lidar
91 system with co-located remote sensing meteorological observations. We supplement this case study with a
92 climatological evaluation using a decade (2015–2024) of routine observations. Our overarching aim is to elucidate
93 the specific role of elevated foehn in driving summer O₃ pollution in Beijing.
94

95 2. Data and method

96 2.1. Observational data

97 Figure 1 shows the observation network and instruments. The network comprises 3 meteorological stations and 46
98 surface O₃ monitoring sites. Among the O₃ sites, 45 are air quality stations operated by the Beijing Municipal
99 Ecological and Environmental Monitoring Center, and one is the Shangdianzi (SDZ) atmospheric background station
100 managed by the Beijing Meteorological Bureau. Two differential absorption O₃ lidars (Hefei GBQ Technology
101 Company) were deployed at the GXT (urban) and SDZ (rural) stations, respectively. These lidars measured O₃
102 profiles with a 5-minute resolution up to an altitude of 3.0 km. In addition, radar wind profilers at GXT, SDZ, as well
103 as Yanqing (YQ) provided continuous wind profiles at 6-minute resolution. Routine meteorological radiosondes
104 launched from the GXT station provided high-vertical-resolution (~10 m) profiles of temperature, relative humidity,
105 wind speed, and wind direction three times daily (08:00, 14:00, and 20:00 BJT) in summer.



106
107 **Figure 1.** Site distribution of surface ozone and meteorological measurements, and ground-based remote sensing
108 instruments used in this study. In (a), dark blue dots denote the GXT, SDZ, and YQ meteorological stations; light
109 blue dots represent the surface ozone observation sites. Panels (b), (c), and (d) show the radar wind profilers at YQ,
110 SDZ, and GXT, ozone lidars at SDZ and GXT, and routine radiosonde instrument at GXT, respectively.
111

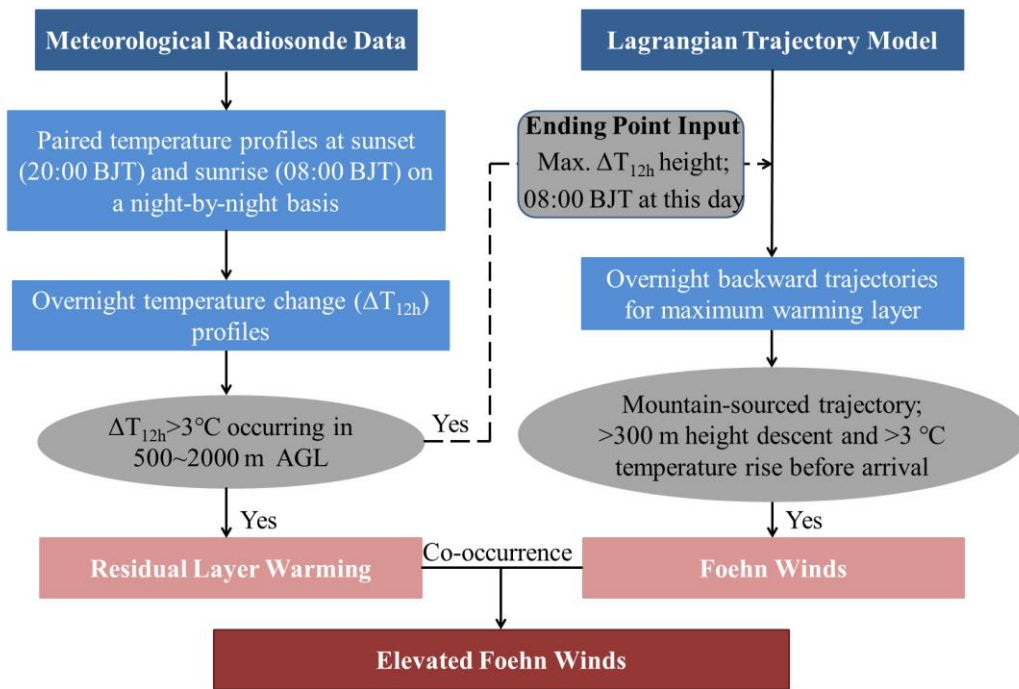
112 To validate the lidar O₃ observations, we compared the lidar-derived O₃ concentration at 300 m height (the lowest
113 reliable altitude above the instrument’s blind zone) with surface measurements. As no surface O₃ data were available
114 at the GXT site, we used measurements from the nearest air quality monitoring station (~2 km away). The validation
115 results demonstrated a strong correlation between the lidar-based and surface-based O₃ concentrations ($R^2 = 0.69$ at
116 GXT and $R^2 = 0.56$ at SDZ), confirming the reliability of the O₃ lidar data (Fig. S1). To construct complete vertical
117 profiles for calculating O₃ transport flux, we used linear interpolation between the surface O₃ measurement and the
118 validated lidar observation at 300 m to fill the blind zone. A similar procedure was applied to patch the blind zone

119 (below 150 m) of the radar wind profiler data, where winds were interpolated between the surface wind observation
 120 and the lowest valid radar measurement at 150 m.

121

122 2.2. Identification of elevated foehn

123 To date, no established method exists for identifying elevated foehn. For the purpose of climatological evaluation,
 124 we develop a framework (Fig. 2) to identify elevated foehn events based on the combination of meteorological
 125 radiosonde data and a Lagrangian trajectory model. First, we calculated overnight temperature change (ΔT_{12h})
 126 profiles by subtracting the radiosonde temperature profiles at 20:00 BJT (sunset) from the profiles at 08:00 BJT the
 127 following day (sunrise) on a night-by-night basis (i.e., $\Delta T_{12h}=T_{08}-T_{20}$). A residual layer warming event was identified
 128 when $\Delta T_{12h}>3^{\circ}\text{C}$ occurred within 500-2000 m AGL layer. This threshold is also commonly used to identify ground-
 129 based foehn elsewhere (Kirchgaessner et al., 2021; Steinhoff et al., 2014). Finally, we examined the backward
 130 trajectory properties (including geographic origin, height change, and temperature change) of the air mass at the
 131 identified maximum warming height (i.e., the height of maximum ΔT_{12h}) using a Lagrangian trajectory model
 132 (Miltenberger et al., 2016). If the 12-h backward trajectory originated from the mountains (azimuth of $250-360^{\circ}$ or
 133 $0-45^{\circ}$, following Li et al. (2025)), and if the trajectory descended more than 300 m accompanied by a temperature
 134 increase exceeding 3°C before arriving in Beijing, we attribute the identified warming case to an elevated foehn
 135 event.



136

137 **Figure 2.** Flowchart for identifying elevated foehn based on the combination of meteorological radiosonde data and
 138 a Lagrangian trajectory model.

139

140 2.3. Supporting calculations and model simulations

141 The boundary layer structure during a diurnal cycle can be classified into three regimes: convective boundary layer
 142 (CBL), stable boundary layer (SBL), and residual layer (RL) (Stull, 1988). We determined the boundary layer height
 143 based on high-resolution radiosonde profiles from the GXT station. Following Liu and Liang (2010), the height of
 144 the CBL (CBLH, at 14:00 BJT) was determined at the base of the overlying temperature inversion capping the
 145 convective thermals. The height of the SBL (SBLH, at 20:00 and 08:00 BJT) was determined at the top of the
 146 underlying temperature inversion, where turbulence nearly ceases. At the morning transition (08:00 BJT), emerging

147 solar radiation gradually erodes the near-surface part of the SBL; thus, the SBLH at this time was determined at the
148 top of the residual underlying temperature inversion. The RL is disconnected from the ground by the underlying SBL
149 but retains the atmospheric state of the former CBL. Its height (RLH) was therefore determined at the base of the
150 overlying temperature inversion at the evening or morning transition (20:00 and 08:00 BJT). For temperature profiles
151 showing no significant overlying inversion, the CHLH and RLH were determined using a multi-variable integrated
152 method proposed by Wang and Wang (2014).

153

154 To analyze O₃ transport in Beijing, we calculated the O₃ transport flux (TF) using collocated wind and O₃ profiles
155 from the GXT and SDZ sites. The transport flux (TF, mg m⁻² s⁻¹), representing the mass flow per unit cross-sectional
156 area per unit time, is determined by the wind speed and the O₃ concentration. The TF at a certain height and direction
157 is calculated as follow:

$$158 \quad TF = C \times WS \times \cos \left[(WD - B) \times \frac{\pi}{180} \right]$$

159 where C represents the O₃ concentration (unit: μg m⁻³), WS denotes the horizontal wind speed (unit: m s⁻¹), WD
160 denotes the horizontal wind direction and B is the azimuth from the start station to the end station. In this study, we
161 calculated O₃ transport flux in the direction from GXT to SDZ. Therefore, positive TF indicates northeastward
162 transport, and negative TF indicates southwestward transport.

163

164 We used the Hybrid Single-Particle Lagrangian Integrated Trajectory (HYSPLIT) model (Stein et al., 2015) to
165 trace the origin and history of the air masses associated with the maximum residual layer warming in Beijing. In
166 addition to HYSPLIT, we employed the Weather Research and Forecasting model with Chemistry (WRF-Chem,
167 version 4.2.1) to simulate O₃ concentrations and meteorological fields. The WRF-Chem model accounts for key
168 atmospheric processes, including emissions, deposition, advection, diffusion, gas-phase chemistry, and aerosol
169 chemistry (Grell et al., 2005). Our simulation domain encompassed most of China, centered at (105.5°E, 37.5°N),
170 with a horizontal grid spacing of 9 km. The meteorological initial and boundary conditions were derived from the
171 National Centers for Environmental Prediction (NCEP) Final Operational Global Analysis data. For emissions, we
172 utilized the Model of Emissions of Gases and Aerosols from Nature (MEGAN) (Guenther et al., 2006) and the Multi-
173 resolution Emission Inventory for China (MEIC) (Zhang et al., 2009), with the latter updated to a 0.1° × 0.1°
174 resolution for 2019 (MEIC-2019; <http://www.meicmodel.org>). The detailed model configuration follows Xu et al.
175 (2024). The WRF-Chem simulation demonstrated a reasonable agreement with observed surface O₃ concentrations
176 during the studied pollution episode ($R^2 = 0.51$ at GXT and $R^2 = 0.44$ at SDZ; Fig. S2).

177

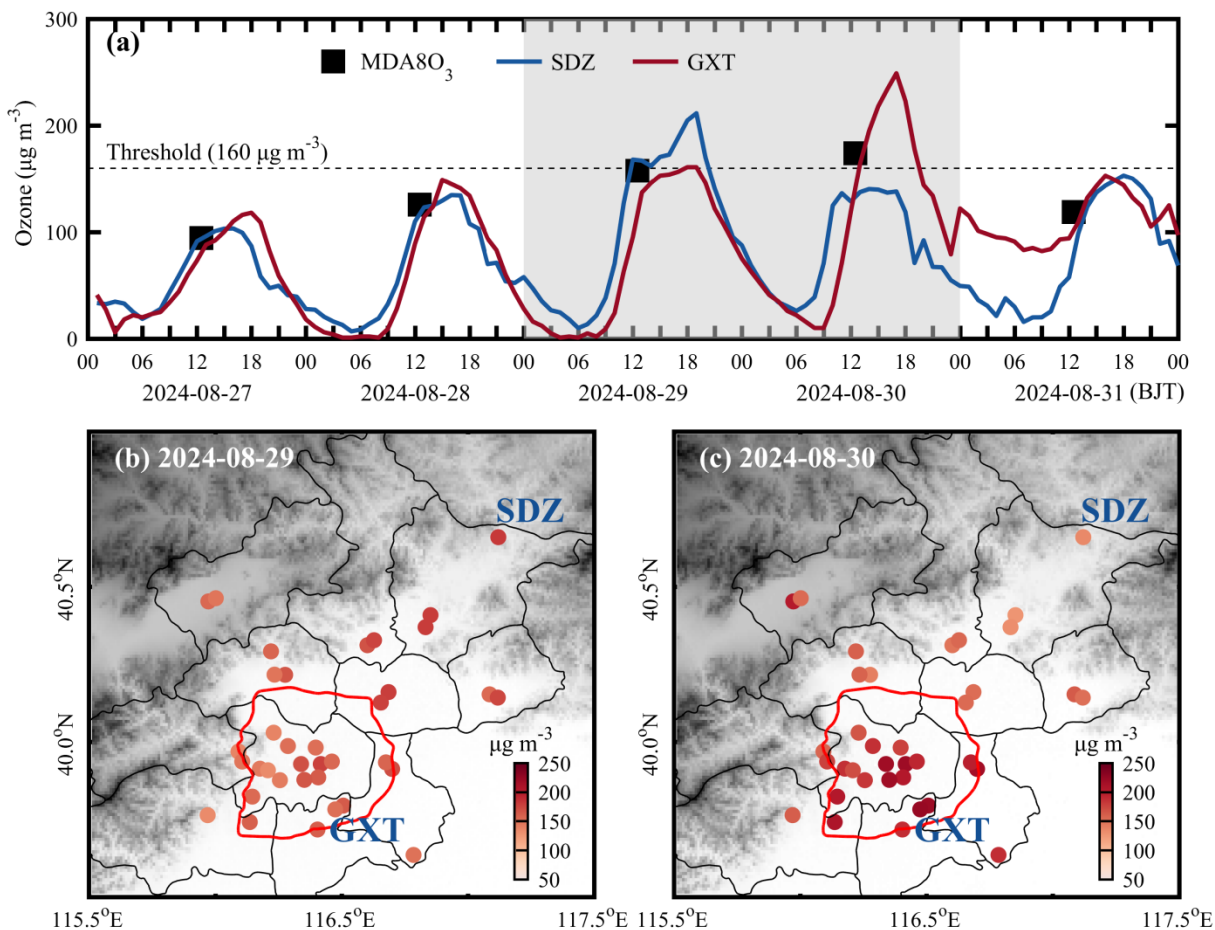
178 **3. Results**

179 **3.1. Case study**

180 **3.1.1. Overview of the O₃ pollution episode**

181 Following heavy rainfall on 26 August 2024, Beijing experienced consecutive sunny days until light rain resumed
182 on 31 August. The persistent sunny weather established favorable meteorological background for photochemical O₃
183 production. Consequently, surface O₃ concentrations in Beijing exhibited a daily increasing trend from 27 to 30
184 August. On the final two days (29 and 30 August), the city-averaged daily maximum 8-hour average O₃ (MDA8O₃)
185 concentrations approached or exceeded China's ambient air quality standard threshold of 160 μg m⁻³, peaking at 174
186 μg m⁻³ on 30 August (Fig. 3a). A notable feature of these two polluted days was the stark contrast in the spatial
187 distribution of O₃ concentrations. On 29 August, the spatial pattern showed a positive O₃ gradient extending
188 northeastward, which was reversed on 30 August (Fig. 3b, c). This contrast was exemplified by the station
189 observations: SDZ recorded its peak O₃ concentration (212 μg m⁻³ at 18:00 BJT) on 29 August, significantly higher

190 than the concurrent value at GXT ($161 \mu\text{g m}^{-3}$). Conversely, GXT observed its maximum O_3 level ($249 \mu\text{g m}^{-3}$ at
 191 16:00 BJT) on 30 August, far exceeding the measurement at SDZ ($138 \mu\text{g m}^{-3}$; Fig. 3a). These contrasting spatial
 192 patterns seem to represent two typical O_3 pollution scenarios in Beijing: an urban plume transport pattern and an
 193 urban pollution accumulation pattern, as previously reported by Zong et al. (2023). The key question is what
 194 mechanism drove the rapid intensification of O_3 pollution and the reversal of its spatial pattern over the two
 195 consecutive days.

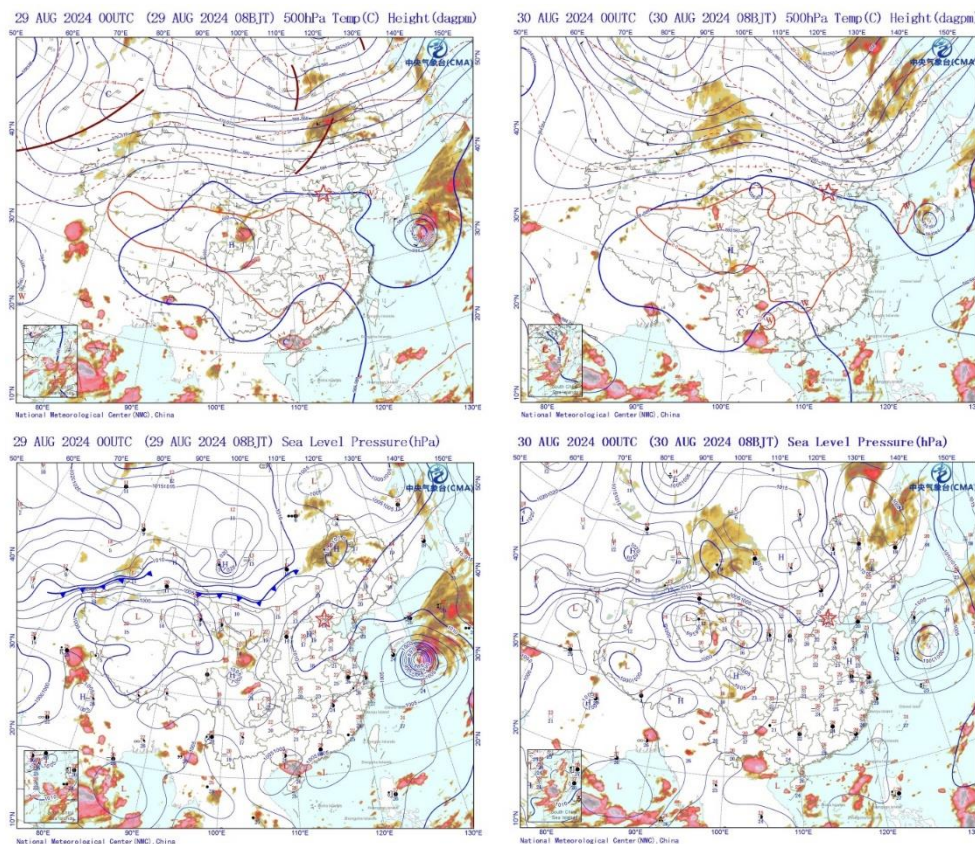


196
 197 **Figure 3.** (a) Time series of surface ozone concentrations at the GXT and SDZ stations from 27 to 31 August 2024;
 198 Spatial distribution of maximum 8-h O_3 concentrations over Beijing on (b) 29 and (c) 30 August. In (a), black squares
 199 represent the city-averaged MDA8O_3 concentrations; gray shading denotes the two polluted days (29 and 30 August
 200 2024).

201
 202 **3.1.2. Meteorological attribution to elevated foehn**

203 The weather charts at 08:00 BJT on 29 and 30 August are presented in Fig. 4. A subtropical high prevailed in the
 204 upper atmosphere over the central and eastern China, while a typhoon was active over the western Pacific Ocean
 205 south of Japan. The coexistence of these two synoptic systems induced widespread clear skies over the eastern China,
 206 a condition highly conducive to photochemical O_3 production (Ouyang et al., 2022; Shu et al., 2016). In the lower
 207 atmosphere, the synoptic patterns differed between the two days. On 29 August, the North China Plain (NCP) was
 208 under the influence of a weak high-pressure system. By 30 August, another high-pressure system (a cold front) had
 209 intruded into the northwestern NCP from the Mongolian Plateau, creating a strong pressure gradient perpendicular
 210 to the Taihang Mountains. Traditionally, cold fronts are known to have a significant clearance effect on air pollutants

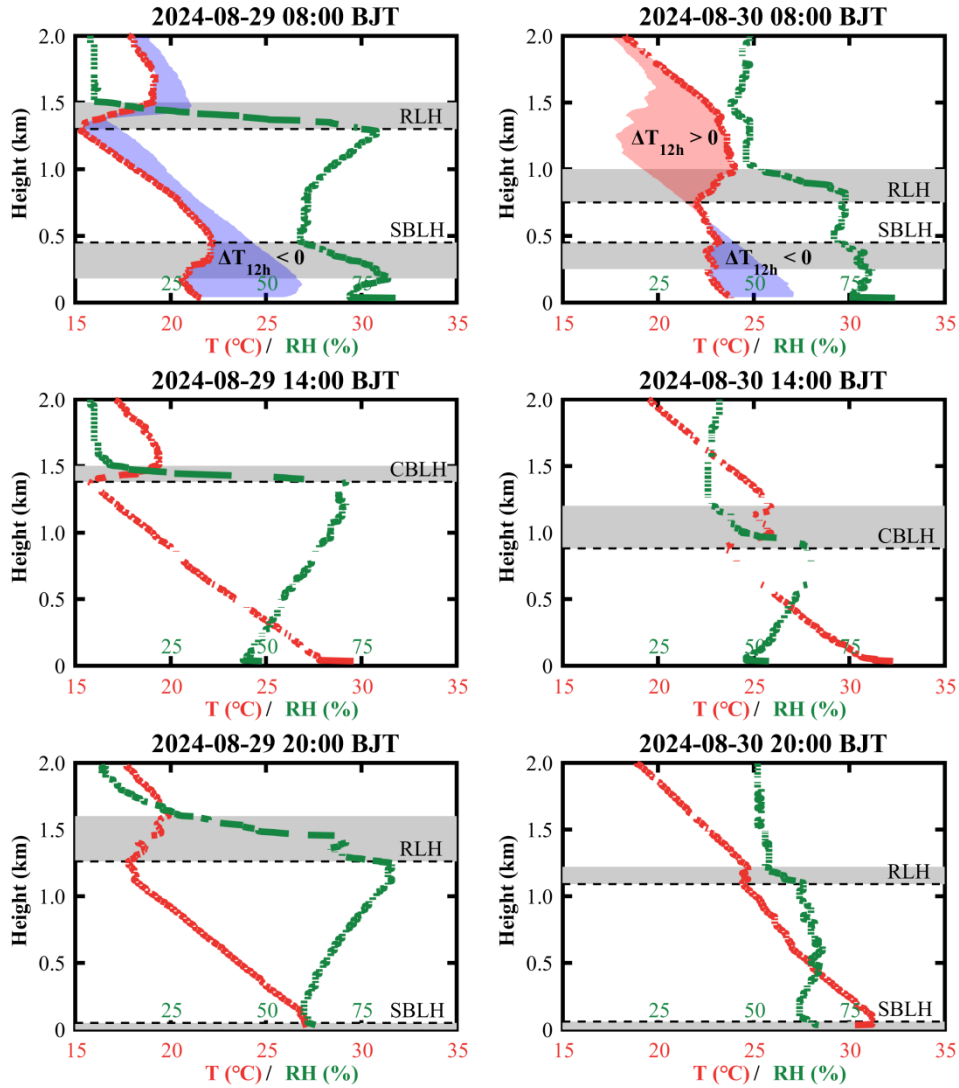
211 (Zhang et al., 2021). However, in this case, the cold front led to an unexpected O₃ increase in Beijing on 30 August.
212 So, what underlying mechanism was responsible for this phenomenon?



213
214 **Figure 4.** Weather charts at 500 hPa and sea-level pressure over the East Asia at 08:00 BJT on 29 and 30 August,
215 2024. Shaded areas denote the cloud cover. The location of Beijing is marked by a red star.
216

217 To address the question above, we examined the radiosonde profiles and derived boundary layer heights at the
218 GXT station (Fig. 5). The results indicate that the CBLH and RLH on 30 August (750, 880, and 1090 m at 08:00,
219 14:00, and 20:00 BJT, respectively) were significantly lower than those on 29 August (1300, 1380, and 1260 m at the
220 same times), despite the SBLH showing no significant difference. The CBLH defines the available volume that the
221 pollutants emitted/produced near the surface can occupy, directly affecting their surface concentration and air quality
222 (Tang et al., 2016). Evidently, the significant decline in CBLH contributes to the surface O₃ enhancements in urban
223 Beijing on 30 August. Notably, the two-day CBLH difference originated from a sharp drop (more than 500 m) in
224 RLH between 20:00 BJT on 29 August and 08:00 BJT on 30 August. Comparing radiosonde profiles from these two
225 time points revealed abnormal drying and warming in the residual layer, with a maximum temperature increase of up
226 to 5.8°C at 1250 m, contrasting sharply with the normal cooling observed the previous night. The base height of this
227 warming layer coincided precisely with the RLH observed at 08:00 BJT on 30 August, indicating that the warming
228 process was responsible for the overnight RLH drop and thereby contributed to the subsequent daytime O₃ pollution
229 exacerbation. Furthermore, the nocturnal residual layer warming inevitably contributes to higher daytime air
230 temperatures. As observed, the afternoon boundary layer temperature on 30 August showed a significant increase
231 compared to the previous afternoon, and this higher temperature further promotes photochemical O₃ production by
232 accelerating photochemical reaction rates and enhancing emissions of volatile organic compounds and soil nitric
233 oxide (Gu et al., 2020; Wu et al., 2024). Thus, in addition to promoting daytime O₃ accumulation by reducing the
234 boundary layer height, residual layer warming also enhances daytime photochemical O₃ production. Moreover, these

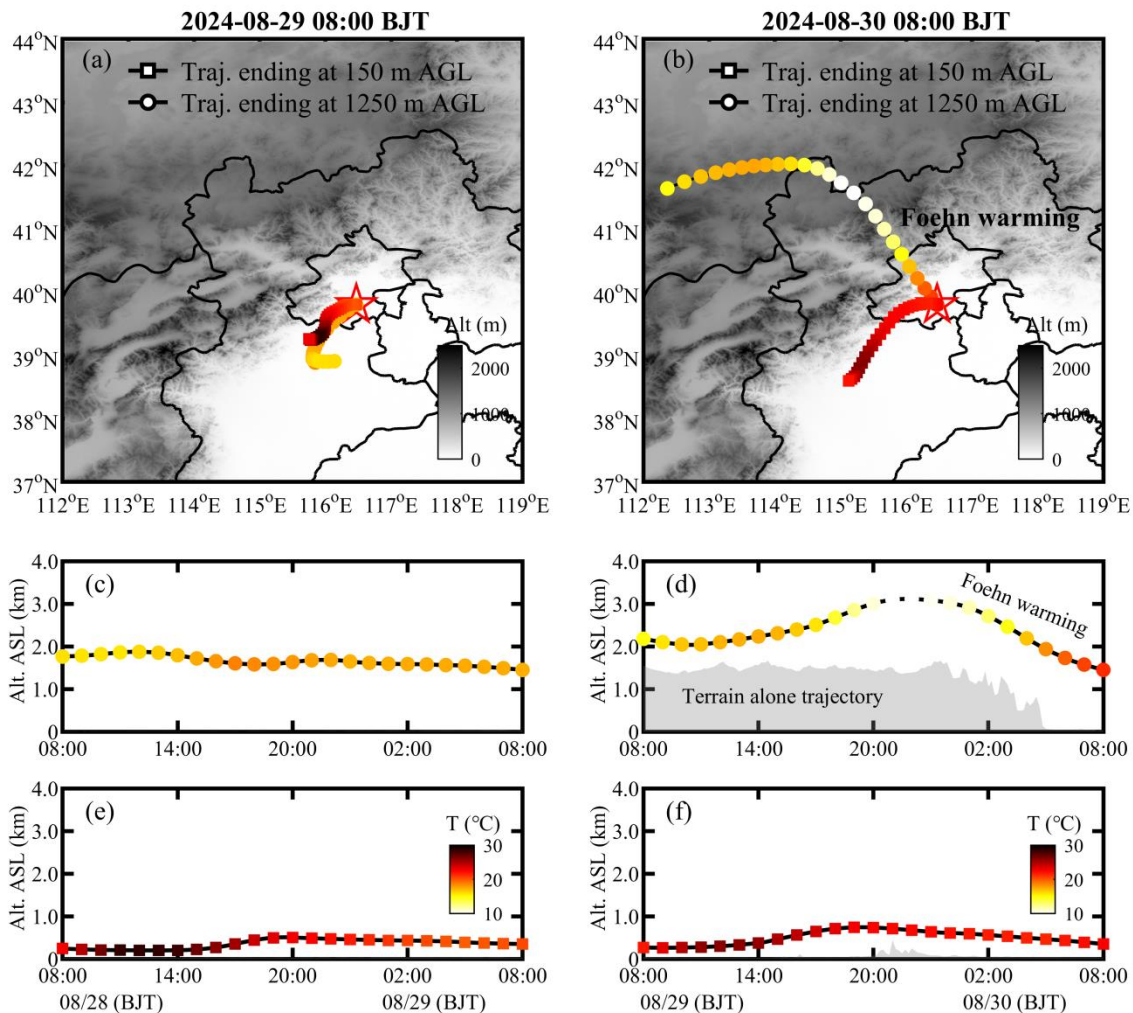
235 changes in boundary layer thermal properties can facilitate O₃ accumulation by lowering O₃ loss. For instance, the
 236 lowered CBLH can reduce the transport of PAN (peroxyacetyl nitrate, a NO_x reservoir in the upper atmosphere) into
 237 urban Beijing (a NO_x-saturated zone), which may suppress O₃ loss from NO titration and independently contribute
 238 to the observed O₃ increases (Flowerday and Hansen, 2026). The remaining question is: what caused the abnormal
 239 warming of the nocturnal residual layer under the background of a cold front intrusion?



240
 241 **Figure 5.** Radiosonde-based temperature (T, red lines) and relative humidity (RH, green lines) profiles at the GXT
 242 station. Gray shaded areas represent the heights of temperature inversion layers. Dashed lines denote the afternoon
 243 convective boundary layer height (CBLH), and dot lines denote the nocturnal stable boundary layer height (SBLH).
 244 Colorful shaded areas highlight the overnight temperature changes, with increase marked in red and decrease in blue.
 245 Note: at 08:00 BJT (morning transition), emerging solar radiation collapses the near-surface SBL; thus, the SBLH at
 246 this time is determined at the top of the residual underlying temperature inversion.

247
 248 Using the HYSPLIT model, we traced the 24-hour origin and characteristics of the air mass at the overnight
 249 maximum warming height (1250 m) observed at 08:00 BJT on 30 August (Fig. 6b and d). For comparison, we also
 250 calculated backward trajectories for the near-surface (150 m) airflow at the same time (Fig. 6b and f), as well as
 251 airflows at the same heights and time on the previous day (Fig. 6a, c, and e). The results show that the airflows at
 252 1250 m and 150 m on 29 August, as well as at 150 m on 30 August, all originated from the southern NCP region with

253 no significant change in trajectory height. In contrast, the air mass at the maximum warming height on 30 August
 254 originated from the Mongolian Plateau. It moved eastward to the northern side of the Yanshan Mountains, turned
 255 southeastward to cross the mountains, and finally arrived in Beijing. During this transport, the airflow first ascended
 256 about 1000 m and then descended about 1500 m, accompanied by a temperature change of cooling (7.6°C) followed
 257 by warming (11.4°C). These changes in trajectory height and temperature exhibit very pronounced foehn warming
 258 characteristics (Elvidge and Renfrew, 2016). Previous studies have reported several cases of shallow foehn-induced
 259 nocturnal surface warming in Beijing (Li et al., 2026; Luo et al., 2020). Our case differs significantly because it
 260 involves elevated air masses and shows no warming in the surface layer. To confirm this, we examined hourly
 261 temperature variations from 20:00 BJT on 29 August to 08:00 BJT on 30 August at 20 surface meteorological stations
 262 in Beijing (Fig. S3), as well as at 15 levels on a 325 m high meteorological tower (Fig. S4). The results revealed that,
 263 except for the high-altitude Foyeding station (1224.9 m), no temperature surges ($\Delta T_{1h} > 1^\circ\text{C}$) were observed before
 264 sunrise (around 06:00 BJT) at the other stations. This implies no detectable foehn warming signature from standard
 265 mountain-lee-side surface observations (Li et al., 2025), despite the strong foehn signature in the residual layer.
 266 Therefore, we identify this case as the first observation of a novel type of foehn phenomenon in Beijing: elevated
 267 foehn in the residual layer.

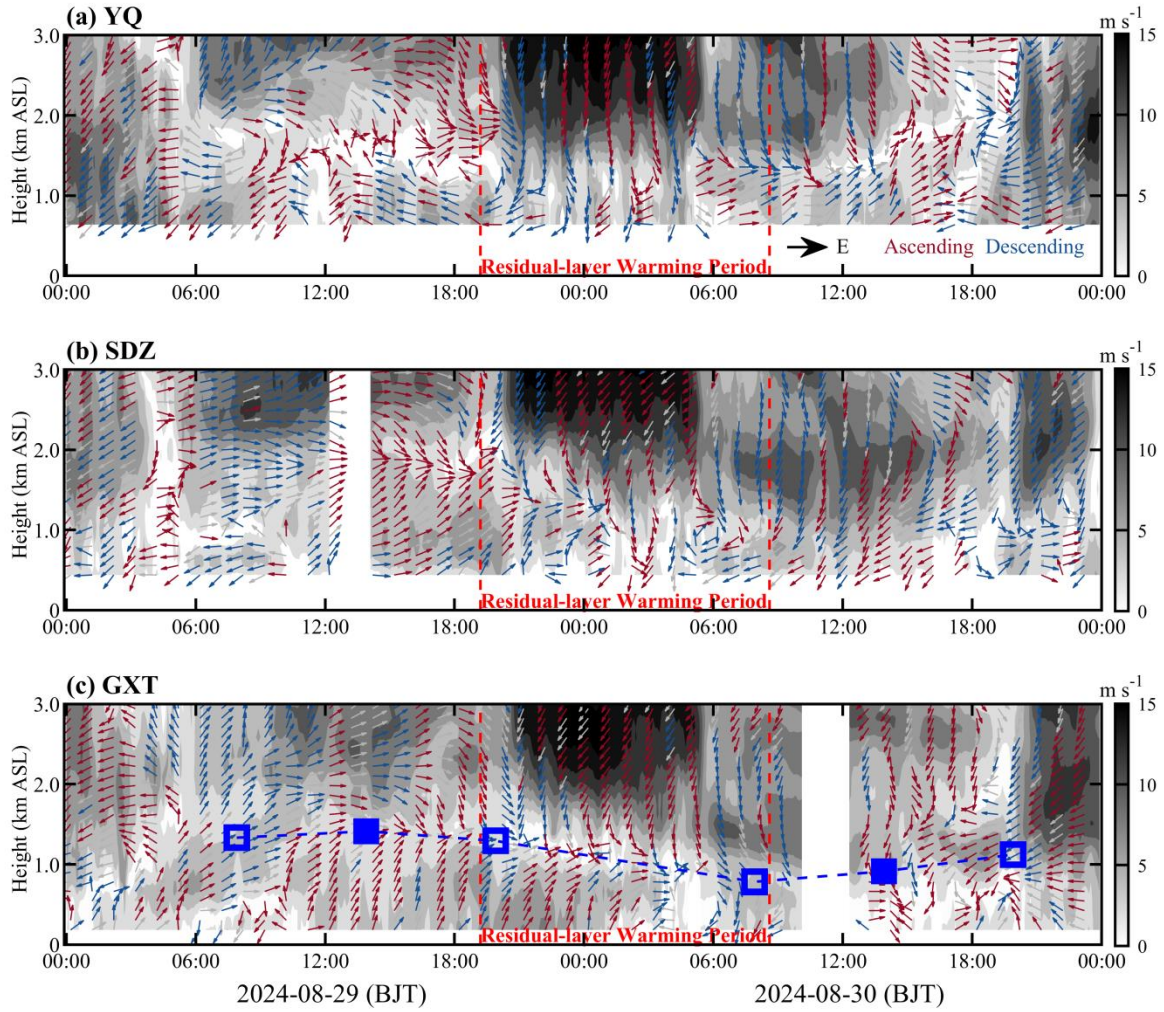


268
 269 **Figure 6.** 24-h backward trajectories ending at 150 m (squares) and 1250 m (dots) above ground level (AGL) over
 270 the GXT station, at 08:00 BJT of (a) 29 and (b) 30 August. The 1250 m level corresponds to the maximum overnight
 271 warming height at 08:00 BJT on 30 August (see Fig. 5). Panels (c-f) show the height and temperature changes of 24-
 272 h backward trajectories at 150 and 1250 m. All temperature changes share the same colorbar, including those in (a)

273 and (b).

274

275 To illustrate the dynamical conditions during the elevated foehn-induced residual layer warming, Figure 7 presents
276 the radar wind profiles at the YQ, SDZ, and GXT stations from 29 to 30 August. Prior to the warming, southerly
277 winds prevailed in the boundary layer (southwesterly at SDZ and GXT; southeasterly at YQ), while lower free-
278 tropospheric winds gradually shifted from southwesterly to northwesterly. After sunset on 29 August, the cold front
279 intrusion induced strong northeasterly winds in the lower free troposphere at all stations. These northeasterly winds
280 aloft first descended into the boundary layer at YQ, followed by SDZ. In contrast, GXT maintained southwesterly
281 boundary-layer winds until later in the night, forming a distinct northwesterly wind shear zone aloft. During this
282 process, the height of the northwesterly wind shear corresponded well with the sounding-derived RLH at GXT, and
283 the northwesterly winds matched the HYSPLIT backward trajectories ending at GXT (Fig. 6b). Combining the
284 HYSPLIT results, these features strongly support the mechanism of an elevated northwesterly foehn during the
285 residual layer warming period. The elevated foehn appears to have occurred within a shallow wind shear zone, similar
286 to the elevated foehn scenario reported in winter Urumqi by Li et al. (2015). After the residual layer warming,
287 northeasterlies prevailed in the boundary layer at SDZ and southwesterlies at YQ, whereas GXT showed highly
288 variable winds with weak speeds—likely due to convergence between the emerging northwesterly foehn and the
289 prevailing southwesterly flows. This weak-wind stagnant condition suppressed the horizontal dispersion of air
290 pollutants. Operating in conjunction with the inhibited vertical dispersion (from a lower boundary layer height) and
291 accelerated photochemical production (due to higher temperatures), this post-foehn convergent stagnation represents
292 a third contributing factor to the severe daytime O₃ pollution observed in urban Beijing on 30 August.



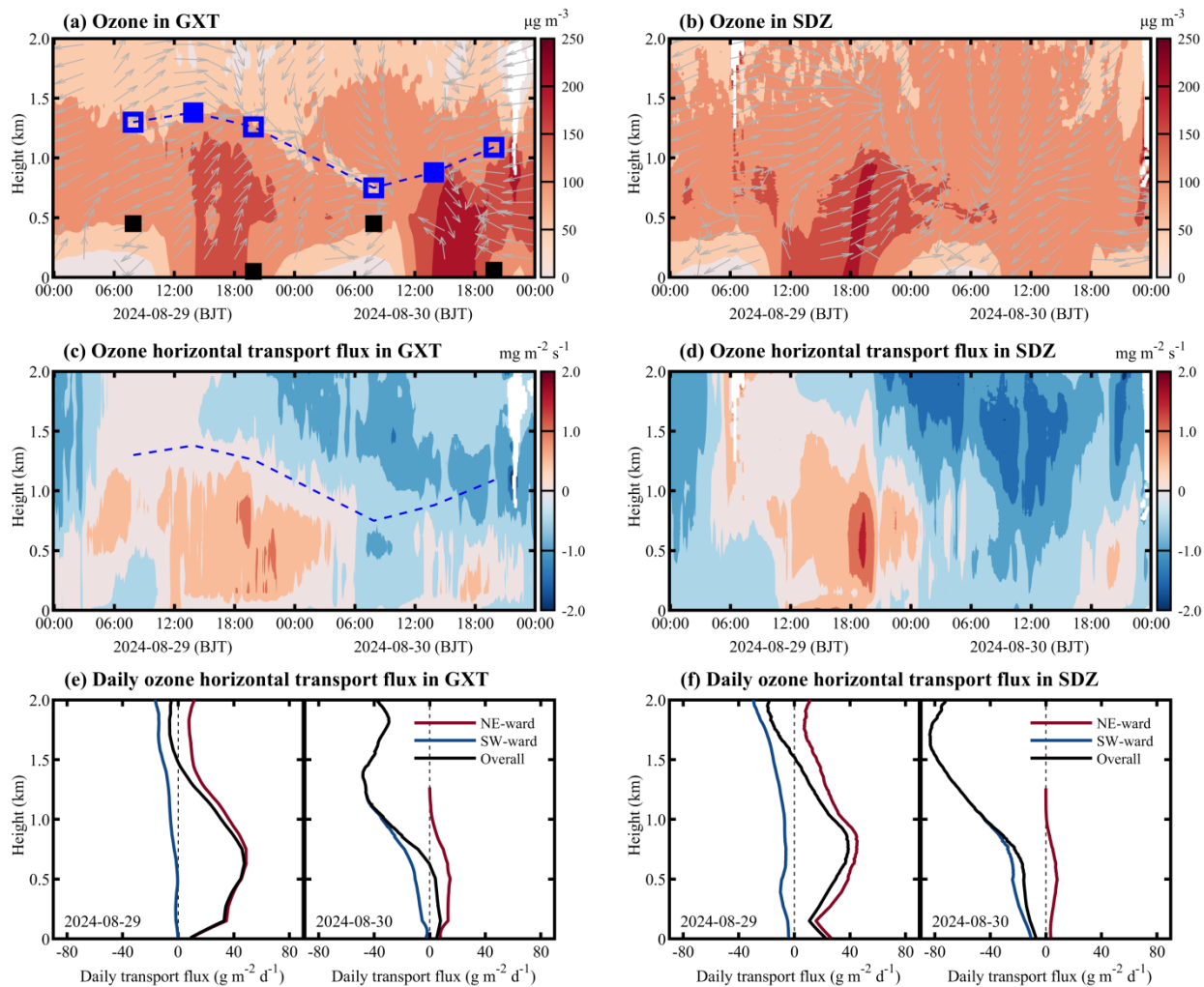
293

294 **Figure 7.** Radar-based wind profiles at the (a) YQ, (b) SDZ, and (c) GXT stations before, during, and after the
 295 elevated foehn-induced residual layer warming. Shaded areas represent horizontal wind speed; arrows denote
 296 horizontal wind direction (red indicates ascending motion, blue indicated descending motion). In (c), blue squares
 297 denote the convective boundary layer height (solid) or residual layer height (hollow); blue dashed line indicates the
 298 evolution of the convective boundary layer and residual layer heights.

299

300 3.1.3. Three-dimensional evolution of O₃ before, during, and after elevated foehn

301 The coordinated O₃ lidar observations at the urban (GXT) and rural (SDZ) stations provided a unique opportunity
 302 to elucidate the three-dimensional evolution of boundary-layer O₃ in response to elevated foehn. By integrating data
 303 from meteorological radiosondes and radar wind profilers, we investigated how sudden changes in boundary layer
 304 thermal and dynamical structure induced by elevated foehn affected O₃ evolution and quantified the differences in
 305 boundary layer O₃ transport fluxes between the pre- and post-foehn days (Fig. 8).



306

307

308

309

310

311

312

313

314

315

316

317

318

319

320

321

322

323

324

325

Figure 8. Vertical O₃ concentrations, wind direction, and O₃ transport flux at the GXT and SDZ stations. In (a), squares denote the boundary layer heights determined from radiosonde profiles (black for SBLH, blue for CBLH/RLH). The blue dashed line in (a) and (c) indicates the evolution of CBL and RL heights. In (c) and (d), positive (negative) horizontal transport flux indicates northeastward (southwestward) transport in the direction from GXT to SDZ. Panels (e) and (f) show the daily integrated O₃ transport flux at the GXT and SDZ stations on 29 and 30 August, respectively.

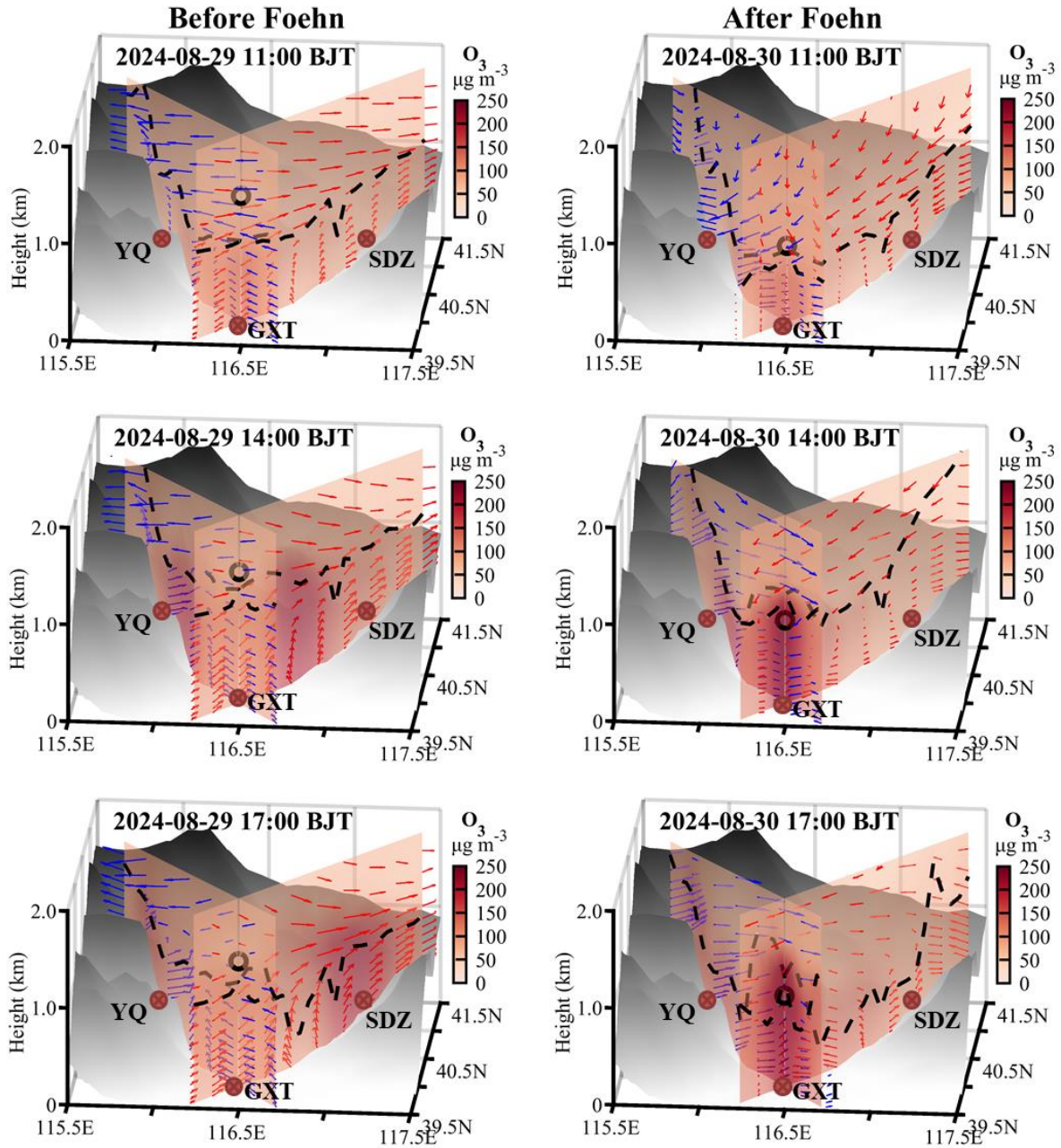
As shown in Fig. 8a, the boundary layer thermal structure critically shaped O₃ vertical distribution in urban Beijing: a steep gradient in the SBL, an O₃ reservoir in the RL, and relatively uniform mixing in the CBL. The elevated foehn-induced residual layer warming on the night of 29–30 August led to a significant reduction in the boundary layer height on 30 August, substantially compressing the vertical space for daytime O₃ mixing. Combined with enhanced photochemical O₃ production (due to higher temperatures) and weakened horizontal dispersion (due to lower post-foehn wind speeds,) these factors collectively contributed to a marked increase in afternoon boundary layer O₃ concentrations in urban Beijing on 30 August (200–250 μg m⁻³) compared to the previous day (~150 μg m⁻³). We also observed that the elevated foehn was accompanied by downward transport of free-tropospheric O₃ (Fig. 8a). However, due to the presence of a strong capping inversion acting as a transport barrier (Fig. 5), this descending free-tropospheric O₃ was unlikely to have significantly intruded into the boundary layer.

The urban-rural coordinated lidar observations clearly reveal a dynamically driven shift in spatial heterogeneity

326 before and after the elevated foehn. On 29 August (pre-foehn), prevailing southwesterly flows facilitated the
327 northeastward transport of the urban O₃ plume. The lidars recorded higher O₃ concentrations at the downwind rural
328 SDZ station than at the urban GXT station (Fig. 8a and b). The peak O₃ occurrence at SDZ was delayed by 1–3 hours
329 relative to GXT, consistent with advective transport. The calculated horizontal O₃ transport flux was predominantly
330 northeastward in the boundary layer at both stations throughout the day, with stronger fluxes in the upper boundary
331 layer. The instantaneous maximum flux at SDZ exceeded 2.0 mg m⁻³ s⁻¹, significantly higher than at GXT (Fig. 8c
332 and d). In stark contrast, the post-foehn convergence stagnation on 30 August suppressed advective transport and
333 promoted local O₃ accumulation in urban Beijing. Consequently, afternoon boundary layer O₃ concentrations at GXT
334 reached notably high levels (200–250 μg m⁻³), while concentrations at SDZ dropped to low values (~100 μg m⁻³).
335 Despite this spatial contrast, the boundary layer O₃ transport flux at both stations was markedly low compared to the
336 previous day (Fig. 8c, d, e, and f), underscoring a shift in the dominant pollution mechanism from urban plume
337 transport to urban pollution accumulation.

338

339 We examined the WRF-Chem output to gain further insight into the vertical O₃ structure over Beijing before and
340 after the elevated foehn. As shown in Fig. 9, although the WRF-Chem model exhibited some deviations in simulating
341 the boundary layer height, it successfully reproduced the pre-foehn northeastward transport of the urban O₃ plume
342 on 29 August, as well as the post-foehn stagnation-driven local O₃ accumulation in the urban Beijing on 30 August.
343 On 29 August, the O₃ pollution initially built up in the urban area (e.g., near GXT) by 11:00 BJT. By 14:00 BJT, the
344 high-O₃ zone had shifted to the northern suburbs, and by 17:00 BJT, it had been transported to the rural areas in the
345 northeast (e.g., near SDZ). In contrast, on 30 August, the relatively higher O₃ concentrations over Beijing were
346 consistently confined in the urban area, with no significant spatial shift. These simulation results aligned well with
347 the lidar observations. Furthermore, the WRF-Chem model reproduced the vertical wind patterns observed at GXT,
348 SDZ, and YQ (Fig. 7), thereby better illustrating the vertical structure of the foehn flow during its decaying stage on
349 30 August via wind cross-sections. The foehn simulations show that while the near-surface component—shallow
350 foehn—was blocked by prevailing southerly winds within the boundary layer, leading to convergence and airflow
351 stagnation over urban Beijing, its upper-layer branch—elevated foehn—passed directly over the urban area
352 unimpeded, resulting in persistent warming that suppressed the daytime convective boundary layer development until
353 the foehn decayed around 14:00 BJT. These features are evident in both the GXT-YQ cross-section (parallel to the
354 elevated northwesterly foehn) and the GXT-SDZ cross-section (perpendicular to the elevated northwesterly foehn).
355 The configuration of an unimpeded elevated foehn and a blocked shallow foehn effectively explains the accumulation
356 of higher O₃ concentrations in the urban boundary layer of Beijing on 30 August.



357

358 **Figure 9.** Cross-sections of simulated O_3 concentrations along the line across the GXT and SDZ stations and the line
 359 across GXT and YQ stations on 29 and 30 August. Dashed black lines denote the simulated boundary layer height,
 360 and arrows show the composite of simulated horizontal wind speed ($m s^{-1}$) and vertical wind speed ($\times 10 m s^{-1}$) in the
 361 GXT-SDZ (red arrows) and GXT-YQ (blue arrows) cross-sections. Only horizontal wind speed in the direction along
 362 the individual cross-sections is included. The black dots denote the boundary layer height observed at GXT and the
 363 height at 14:00 BJT is the observational value and these at 11:00 and 17:00 BJT are interpolated from two adjacent
 364 radiosonde observations.

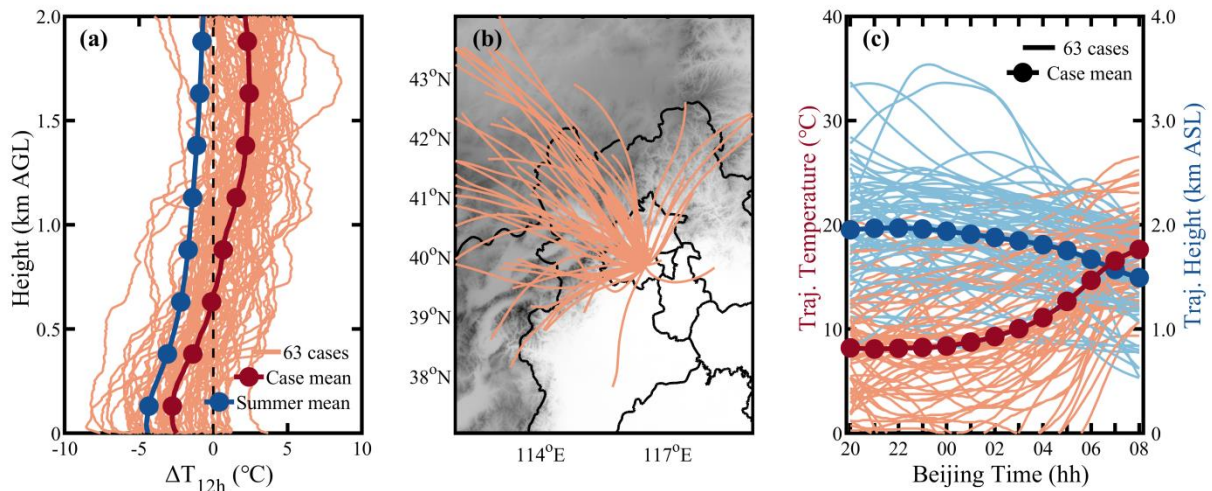
365

366 3.2. Climatological evaluation

367 While a case study is valuable for mechanistic understanding, the question of representativeness always arises. To
 368 clarify whether the features identified in the case study are typical, we supplemented the case analysis with a
 369 climatological investigation of elevated foehn and its O_3 pollution effect based on long-term observations.

370

371 Based on summer radiosonde data from the GXT station during 2015-2024, we calculated overnight temperature
 372 change (ΔT_{12h}) profiles for each night by differencing the temperature profiles at 20:00 BJT and 08:00 BJT the
 373 following day. We identified a residual layer warming event when $\Delta T_{12h} > 3^\circ\text{C}$ occurred within 500-2000 m height
 374 range. For each event, we identified the height of maximum warming and used it as the endpoint for backward
 375 trajectory calculations. Statistical results show that among the 920 valid summer observation days from 2015 to 2024,
 376 a total of 63 residual layer warming cases were identified, accounting for 6.85% of summer night. Figure 10 illustrates
 377 the ΔT_{12h} profiles, backward trajectories, and trajectory height/temperature changes for these events. While warming
 378 heights vary widely across different events, the composite ΔT_{12h} profile highlights warming above ~ 650 m,
 379 contrasting sharply with the summer mean profile showing nocturnal cooling throughout the layer. The backward
 380 trajectories of these warming air masses show that most originated from high-altitude regions to the west or north.
 381 After crossing the Yanshan or Taihang Mountains, these airflows arrived in Beijing, with their trajectories descending
 382 on average by 500 m and their temperature rising rapidly by an average of 10°C , exhibiting clear foehn characteristics.
 383 Applying the elevated foehn criteria from Sect. 2.2, 54 of the 63 warming cases (85.7%) can be attributed to elevated
 384 foehn. These results confirm that elevated foehn is the primary cause of nocturnal residual layer warming in Beijing.

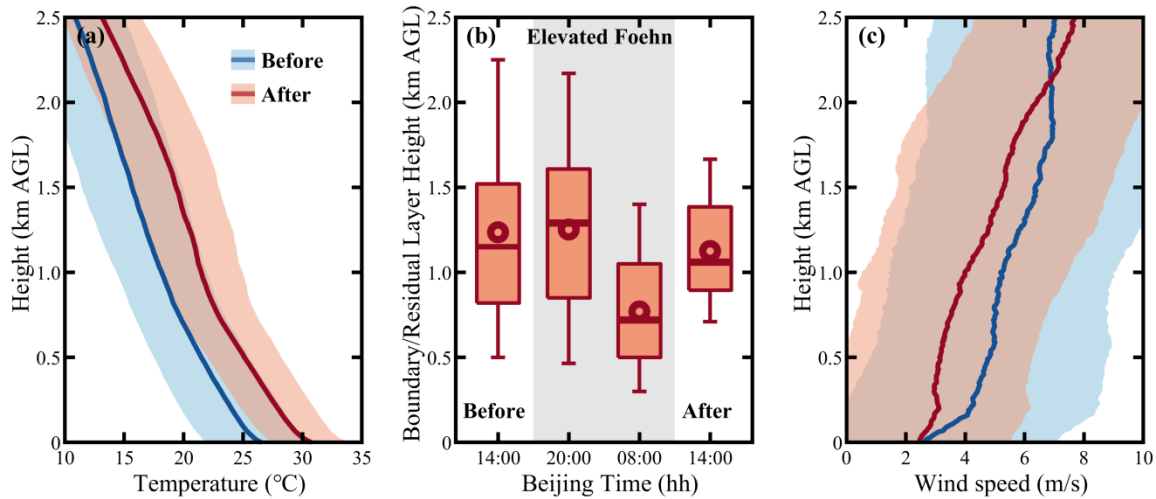


385

386 **Figure 10.** (a) Overnight temperature change (ΔT_{12h}) profiles from 20:00 BJT to next-day 08:00 BJT, (b) overnight
 387 airflow backward trajectories ending at the maximum warming height, and (c) overnight trajectory height and
 388 temperature changes for the 63 identified residual layer warming events.

389

390 Previous case analysis indicated that elevated foehn exacerbates next-day O_3 pollution through three pathways:
 391 increasing boundary layer temperature (enhancing photochemistry), reducing boundary layer height (inhibiting
 392 vertical diffusion), and weakening boundary layer winds (suppressing horizontal dispersion). Composite analyses of
 393 all 54 elevated foehn events (Fig. 11) strongly support the prevalence of these mechanisms. On average, post-foehn
 394 afternoon boundary layer temperature was more than 3°C higher than pre-foehn conditions. The elevated foehn-
 395 induced residual layer warming directly led to an average RLH reduction of 480 m, and the subsequent afternoon
 396 CBLH was, on average, 110 m lower. Post-foehn afternoon boundary layer wind speed decreased by more than 1.0
 397 m s^{-1} on average. Overall, these meteorological changes consistently favor local O_3 production and accumulation. As
 398 a result, approximately 87% of elevated foehn events were followed by worsened O_3 pollution. Post-foehn MDA8O_3
 399 concentrations across Beijing increased by an average of 20–60% (varying by site) compared to the preceding day
 400 (Fig. 12b). Within the main urban zone (inside the 6th Ring Road), the MDA8O_3 increase generally exceeded 45%
 401 (Fig. 12b), with concentrations commonly surpassing the national air quality standard of $160 \mu\text{g m}^{-3}$ (Fig. 12a).



402

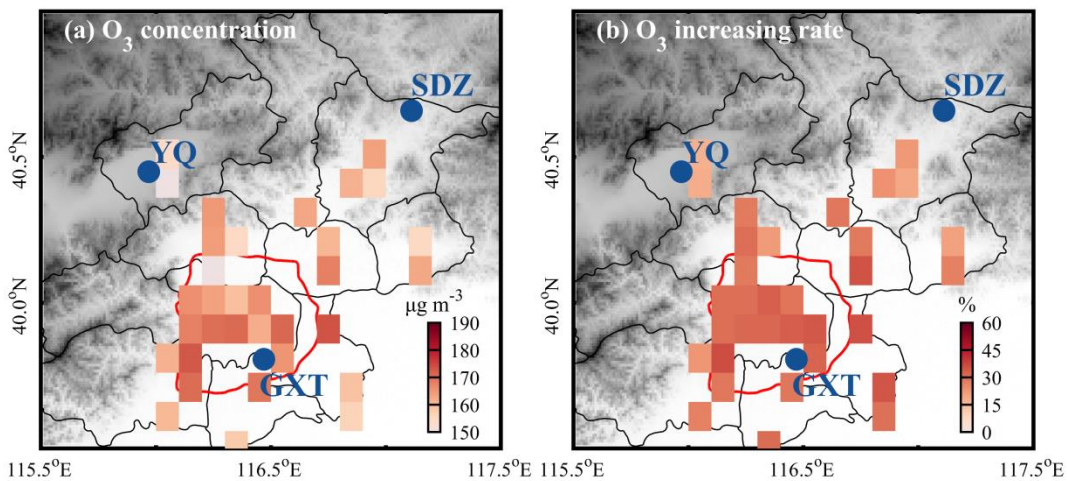
403

404

405

406

Figure 11. Composite of (a) afternoon boundary layer temperature profiles, (b) boundary/residual layer height, and (c) afternoon boundary layer wind speed profiles before, during, and after 54 identified elevated foehn events in Beijing. In (a) and (c), solid lines denote the mean profiles and shaded areas represent the standard deviation. In (b), box-and-whisker plots show the 5th, 25th, 50th, 75th, and 95th percentiles; dots represent the means.



407

408

409

410

411

412

Figure 12. Composite of (a) daily maximum 8-h O_3 concentrations following elevated foehn in Beijing, and (b) their average percentage increase compared to preceding days. Note: site data are resampled and shown on a $0.1^\circ \times 0.1^\circ$ grid, accounting for the relocation of some sites around 2021.

4. Discussion

413

414

415

416

417

418

419

420

421

Traditionally, nocturnal warming has been considered rare. Previous studies have observed occasional nighttime surface warming in leeward plains or valleys due to foehn effects (Luo et al., 2020; Ma et al., 2015). This study, by creatively integrating radiosonde data, reveals for the first time the frequent occurrence of pronounced nocturnal residual layer warming in summer Beijing. The primary driver is identified as elevated foehn—an upper-layer phenomenon previously missed by near-surface observations. Theoretically, unlike near-surface warming from shallow foehn (which enhances boundary layer instability), residual layer warming from elevated foehn reinforces static stability (Stull, 1988). Our observations show that the elevated foehn-induced warming substantially lowers the boundary layer capping inversion (i.e., RLH), thereby inhibiting the development of the next day's convective boundary layer. While Pal and Lee (2019) highlighted that mountain air mass advection can lead to boundary layer

422 overrunning over downwind plains, our results demonstrate that under elevated foehn, mountain-sourced air masses
423 can instead act to lower the downwind boundary layer height through foehn warming.

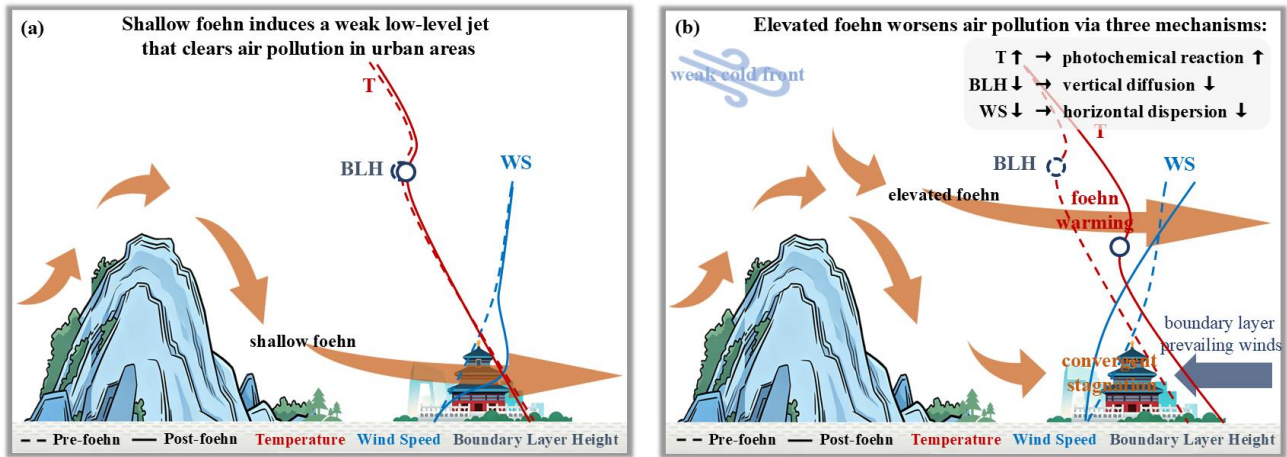
424

425 The elevated foehn process in summer Beijing shows both similarities and differences with that in winter Urumqi
426 (Li et al., 2015). The similarity lies mainly in the three-layer flow structure that causes similar "sandwich" foehn
427 warming within a middle wind shear layer. The key difference lies in the post-foehn boundary layer convergence
428 mechanism. In winter Urumqi, a downslope wind and hydraulic jump occur simultaneously on the northern leeside
429 of the Tianshan Mountains after the foehn encounters a cold air pool in the southern suburbs, generating convergence
430 between the cold pool and the shallow downslope wind (Li et al., 2015). In contrast, no such cold air pool exists in
431 summer Beijing. Here, the post-foehn convergence instead results from the confrontation between the emerging
432 northwestern foehn winds and the prevailing southwestern winds within the boundary layer. The relatively strong
433 boundary-layer southwesterly winds appear to be a necessary prerequisite for the occurrence of elevated foehn in
434 summer Beijing, as they inhibit the intrusion of shallow foehn toward plain areas and, in turn, force the foehn to
435 develop upward. In other words, the relatively strong boundary-layer southwesterly winds in summer Beijing likely
436 play a role similar to that of the cold air pool in winter Urumqi in lifting the foehn to form an elevated foehn.

437

438

439 Our results reveal that 86.9% of the identified elevated foehn events were followed by O₃ pollution exacerbation
440 in summer Beijing. Post-foehn MDA8O₃ concentrations increased more than 30% on average, exceeding the national
441 pollution threshold at most monitoring sites. In a previous study, Li et al. (2025) explored connections between
442 ground-based (shallow) foehn and PM_{2.5} pollution in Beijing, finding that 60.4 % of cases corresponded to pollution
443 mitigation and only 39.6% to exacerbation. Given that direct comparability is limited due to differences in pollutant
444 (PM_{2.5} vs. O₃), season (annual vs. summer), and foehn type (shallow vs. elevated), we acquired the summertime
445 shallow foehn dates identified in Li et al. (2025) and conducted additional statistics of air pollution for summertime
446 shallow foehn events (Table S1). The statistics indicated that elevated foehn corresponds to a markedly higher
447 probability (86.9%) of post-foehn O₃ pollution exacerbation compared to shallow foehn (55.2%). Similar results are
448 found for PM_{2.5} pollution (69.8% vs. 55.2%). These results clearly indicate that elevated foehn exhibits a more
449 deterministic pollution-worsened effect than shallow foehn. Furthermore, we examined the changes in boundary layer
450 structure before and after summertime shallow foehn events (Fig. S5). The results revealed no significant changes in
451 boundary layer temperature or boundary layer height. However, shallow foehn tends to induce a weak low-level jet,
452 which can clear air pollution in urban areas and thereby inhibit pollution exacerbation. In light of the above
453 comparison, we summarized a conceptual diagram in Fig. 13 to illustrate the distinct pollution mechanisms associated
454 with shallow versus elevated foehn. Overall, elevated foehn can serve as a more reliable meteorological precursor
455 for O₃ pollution warnings in summer Beijing. Since elevated foehn can be directly identified from routine radiosonde
456 observations (Sect. 2.2), its application as a precursor for summer O₃ forecasting can be both highly convenient and
457 timely.



458

459

460

461

462

Figure 13. Conceptual diagram illustrating the distinct pollution mechanisms associated with shallow versus elevated foehn.

462

5. Conclusion

463

This study systematically investigated the formation process of elevated foehn winds and their mechanisms for exacerbating surface O_3 pollution in summer Beijing through a combined case analysis and climatological evaluation. The main conclusions are as follows:

464

465

466

467

468

469

470

471

472

473

474

475

476

477

478

479

480

481

482

483

484

485

486

487

488

489

490

- 1、 First observational confirmation of elevated foehn events in summer Beijing. Utilizing high-resolution radiosonde observations, this study identified a novel phenomenon distinct from traditional near-surface foehn. It manifests as abnormal nocturnal warming ($\Delta T_{12h} > 3^\circ C$) within the elevated residual layer (approximately 500–2000 m AGL), with no significant warming signal at the surface. Lagrangian back-trajectory analysis confirms that the warming air masses originate from the northwestern or northern plateaus, undergoing descent and warming after crossing the Yanshan or Taihang Mountains, exhibiting classic foehn characteristics. These elevated foehn events account for 5.87% of summer nights and are identified as the primary driver (85.7% of identified cases) of nocturnal residual layer warming in Beijing.
- 2、 Clarification of the triple synergistic mechanisms through which elevated foehn exacerbates next-day O_3 pollution. Thermodynamic Effect I: Increasing boundary layer temperature to enhance photochemical production. Nocturnal residual layer warming directly leads to a significantly higher daytime boundary layer temperature (average increase $> 3^\circ C$), accelerating the photochemical reaction rates of precursors. Thermodynamic Effect II: Lowering the boundary layer height to suppress vertical diffusion. The residual layer warming reinforces atmospheric stability, causing the capping inversion base (i.e., the residual layer height) to drop by an average of ~ 480 m and the subsequent afternoon convective boundary layer height to decrease by ~ 110 m. This substantially compresses the vertical mixing volume for pollutants. Dynamic Effect: Inducing boundary-layer convergent stagnation to weaken horizontal transport. The intruding northwesterly elevated foehn flow confronts the prevailing southwesterlies within the boundary layer, forming a convergence zone. This leads to a marked reduction in wind speed (average decrease $> 1.0 \text{ m s}^{-1}$), severely hindering the horizontal advective dispersion of pollutants.
- 3、 Decade-long climatological evaluation confirms the highly deterministic and prevalent exacerbating effect of elevated foehn on summer O_3 pollution. Composite analysis of 54 identified elevated foehn events from 2015–2024 robustly supports the proposed mechanisms. Statistics show that 87% of elevated foehn events were followed by worsened O_3 pollution the next day. The city-wide $MDA8O_3$ concentration increased by 20–60% on average compared to the preceding day, with increases in the main urban area typically exceeding 45%. Post-

491 foehn MDA8O₃ concentrations commonly surpassed the national ambient air quality standard (160 µg m⁻³). This
492 stands in sharp contrast to additional statistics based on near-surface observations, which associate shallow foehn
493 primarily with no significant pollution changes, highlighting the fundamental difference in pollution potential
494 between shallow and elevated foehn.

495
496 In summary, this study identifies elevated foehn as a significant and previously overlooked meteorological forcing
497 factor for summer O₃ pollution in Beijing. Its synergistic "warming-lowering-stagnating" effects lead to a highly
498 deterministic pollution exacerbation. Given that elevated foehn can be directly identified using routine radiosonde
499 data, we propose its utility as a reliable and efficient meteorological precursor for O₃ pollution forecasting and
500 warning in Beijing and other cities with similar topography. This provides a new scientific basis for the precise
501 prevention and control of air pollution. Future research should focus on quantifying the contribution of elevated foehn
502 to O₃ generation under different synoptic backgrounds and exploring its coupling with regional transport and
503 chemical processes.

504
505 To date, numerous circulation classification-based studies have highlighted the importance of synoptic-scale
506 weather on regional O₃ pollution in the NCP region (Dong et al., 2020; Han et al., 2020; Liao et al., 2024; Liu et al.,
507 2019). However, day-to-day circulation classifications actually overlook sub-daily meteorological processes, such as
508 the nocturnal elevated foehn identified in this study. A very recent study (Xu et al., 2026) indicated that ground-based
509 foehns on the eastern Taihang Mountains preferentially occur under stable atmospheric stratification, with a surface
510 high over the windward side and a low over the leeward side, together with an upper-level cold trough at 500 hPa
511 and pronounced subsidence at 850 hPa on the leeward side on the eastern foothills of the Taihang Mountains.
512 However, this study did not extend its findings to the field of air pollution, nor did it clarify whether the
513 aforementioned synoptic conditions are also conducive to the occurrence of elevated foehn. Overall, a better coupling
514 of synoptic-scale circulation patterns and local-scale elevated foehn processes will further deepen our understanding
515 of meteorological mechanisms underlying O₃ pollution.

516 ***Code and data availability***

517
518 Hourly surface ozone data, except for those from the SDZ station, were obtained from the China National
519 Environmental Centre (<http://www.cnemc.cn/en/>). The HYSPLIT model and its compatible meteorological data were
520 sourced from the NOAA Air Resources Laboratory (<https://www.ready.noaa.gov/HYSPLIT.php>). We are not
521 authorized to publicly release the following raw data: hourly ozone measurements at the SDZ station, radiosonde
522 data, ozone lidar observations, wind profiler radar measurements, and numerical simulation outputs. These datasets
523 are available from the corresponding author upon reasonable request (zqma@ium.cn).

524 **Author contributions**

525
526 Z.L. conceived the original idea, analyzed the data, and wrote the first version manuscript. J.X. conducted the WRF-
527 Chem simulation. L.Z. operated the remote sensing equipment. C.L. performed the HYSPLIT model. Z.M. supervised
528 the research project. All authors discussed the results and commented on the manuscript.

529 **Competing interests**

530
531 The authors declare no competing interests.

532 **Acknowledgements**

533
534 This research has been supported by the National Natural Science Foundation of China (Grant Nos. 42405115 and

535 42307150), and the Scientific Research Project of the Beijing Meteorological Bureau (Grant No. BMBKJ202404002).
536 We acknowledge the DeepSeek for polishing our English language. We thank the two anonymous reviewers for their
537 comments, which have greatly improved the quality of the manuscript.

538

539 **References**

- 540 Baumann, K., Maurer, H., Rau, G., Piringer, M., Pechinger, U., Prévôt, A., Furger, M., Neininger, B., Pellegrini, U.: The
541 influence of south Foehn on the ozone distribution in the Alpine Rhine valley—results from the MAP field phase, *Atmos.*
542 *Environ.*, 35, 6379-6390, [https://doi.org/10.1016/S1352-2310\(01\)00364-8](https://doi.org/10.1016/S1352-2310(01)00364-8), 2001.
- 543 Campana, M., Li, Y., Staehelin, J., Prevot, A.S.H., Bonasoni, P., Loetscher, H., Peter, T.: The influence of south foehn on
544 the ozone mixing ratios at the high alpine site Arosa, *Atmos. Environ.*, 39, 2945-2955,
545 <https://doi.org/10.1016/j.atmosenv.2005.01.037>, 2005.
- 546 Dong, Y.M., Li, J., Guo, J.P., Jiang, Z.J., Chu, Y.Q., Chang, L., Yang, Y., Liao, H.: The impact of synoptic patterns on
547 summertime ozone pollution in the North China Plain, *Sci. Total Environ.*, 735, 139559,
548 <https://doi.org/10.1016/j.scitotenv.2020.139559>, 2020.
- 549 Elvidge, A.D. and Renfrew, I.A.: The Causes of Foehn Warming in the Lee of Mountains, *B. Am. Meteor. Soc.*, 97, 455-
550 466, <https://doi.org/10.1175/BAMS-D-14-00194.1>, 2016.
- 551 Flowerday, C. and Hansen, J.C.: Peroxyacetyl Nitrate (PAN) in the Atmosphere: A Comprehensive Review of Chemistry,
552 Measurements, and Chemical-Transport Implications, *Environ. Sci.: Atmos.*, <https://doi.org/10.1039/D6EA00017G>, 2026.
- 553 Gaffin, D.M.: Unexpected Warming Induced by Foehn Winds in the Lee of the Smoky Mountains, *Wea. Forecasting*, 17,
554 907-915, [https://doi.org/10.1175/1520-0434\(2002\)017<0907:UWIBFW>2.0.CO;2](https://doi.org/10.1175/1520-0434(2002)017<0907:UWIBFW>2.0.CO;2), 2002.
- 555 Gaffin, D.M.: On High Winds and Foehn Warming Associated with Mountain-Wave Events in the Western Foothills of the
556 Southern Appalachian Mountains, *Wea. Forecasting*, 24, 53-75, <https://doi.org/10.1175/2008WAF2007096.1>, 2009.
- 557 Grell, G.A., Peckham, S.E., Schmitz, R., McKeen, S.A., Frost, G., Skamarock, W.C., Eder, B.: Fully coupled “online”
558 chemistry within the WRF model, *Atmos. Environ.*, 39, 6957-6975, <https://doi.org/10.1016/j.atmosenv.2005.04.027>, 2005.
- 559 Gu, Y., Li, K., Xu, J., Liao, H., Zhou, G.: Observed dependence of surface ozone on increasing temperature in Shanghai,
560 China, *Atmos. Environ.*, 221, 117108, <https://doi.org/10.1016/j.atmosenv.2019.117108>, 2020.
- 561 Guenther, A., Karl, T., Harley, P., Wiedinmyer, C., Palmer, P.I., Geron, C.: Estimates of global terrestrial isoprene emissions
562 using MEGAN (Model of Emissions of Gases and Aerosols from Nature), *Atmos. Chem. Phys.*, 6, 3181-3210,
563 <https://doi.org/10.5194/acp-6-3181-2006>, 2006.
- 564 Han, H., Liu, J.E., Shu, L., Wang, T.J., Yuan, H.L.: Local and synoptic meteorological influences on daily variability in
565 summertime surface ozone in eastern China, *Atmos. Chem. Phys.*, 20, 203-222, <https://doi.org/10.5194/acp-20-203-2020>,
566 2020.
- 567 Kerr, R.A.: Chinook Winds Resemble Water Flowing over a Rock, *Science*, 231, 1244-1245,
568 <https://doi.org/10.1126/science.231.4743.1244>, 1986.
- 569 Kirchgaessner, A., King, J.C., Anderson, P.S.: The Impact of Föhn Conditions Across the Antarctic Peninsula on Local
570 Meteorology Based on AWS Measurements, *J. Geophys. Res.-Atmos.*, 126, e2020JD033748,
571 <https://doi.org/10.1029/2020JD033748>, 2021.
- 572 Li, J., Sun, Z., Lenschow, D.H., Zhou, M., Dou, Y., Cheng, Z., Wang, Y., Li, Q.: A foehn-induced haze front in Beijing:
573 observations and implications, *Atmos. Chem. Phys.*, 20, 15793-15809, <https://doi.org/10.5194/acp-20-15793-2020>, 2020a.
- 574 Li, J., Zhang, J., Bai, M., Su, J., Li, Q., Jia, X.: Identification and characterization of foehn events in Beijing and their
575 impact on air pollution episodes, *Atmos. Chem. Phys.*, 25, 8683-8700, <https://doi.org/10.5194/acp-25-8683-2025>, 2025.
- 576 Li, X., Xia, X., Wang, L., Cai, R., Zhao, L., Feng, Z., Ren, Q., Zhao, K.: The role of foehn in the formation of heavy air
577 pollution events in Urumqi, China, *J. Geophys. Res.-Atmos.*, 120, 5371-5384, <https://doi.org/10.1002/2014JD022778>,
578 2015.

579 Li, X., Xia, X., Zhong, S., Luo, L., Yu, X., Jia, J., Zhao, K., Li, N., Liu, Y., Ren, Q.: Shallow foehn on the northern leeward
580 of Tianshan Mountains and its influence on atmospheric boundary layer over Urumqi, China – A climatological study,
581 *Atmos. Res.*, 240, 104940, <https://doi.org/10.1016/j.atmosres.2020.104940>, 2020b.

582 Li, Y., Chen, M., Miao, S., Zhang, G., Huang, Q., Zhang, S.: Evaluation of three scale-aware planetary boundary layer
583 schemes in WRF Model during Beijing 2022 Winter Olympics, *Atmos. Res.*, 328, 108416,
584 <https://doi.org/10.1016/j.atmosres.2025.108416>, 2026.

585 Liao, Z., Pan, Y., Ma, P., Jia, X., Cheng, Z., Wang, Q., Dou, Y., Zhao, X., Zhang, J., Quan, J.: Meteorological and chemical
586 controls on surface ozone diurnal variability in Beijing: A clustering-based perspective, *Atmos. Environ.*, 295, 119566,
587 <https://doi.org/10.1016/j.atmosenv.2022.119566>, 2023.

588 Liao, Z., Sun, J., Yao, J., Liu, L., Li, H., Liu, J., Xie, J., Wu, D., Fan, S.: Self-organized classification of boundary layer
589 meteorology and associated characteristics of air quality in Beijing, *Atmos. Chem. Phys.*, 18, 6771-6783,
590 <https://doi.org/10.5194/acp-18-6771-2018>, 2018.

591 Liao, Z.H., Jia, X.C., Qiu, Y.L., Quan, J.N., Pan, Y.B., Ma, P.K., Cheng, Z.G., Wang, Q.Q.: Synoptic controls on warm-
592 season O₃ pollution in eastern China: A focus on O₃-NO_x-VOC chemistry, *Atmos. Res.*, 311, 107660,
593 <https://doi.org/10.1016/j.atmosres.2024.107660>, 2024.

594 Liu, J.D., Wang, L.L., Li, M.G., Liao, Z.H., Sun, Y., Song, T., Gao, W.K., Wang, Y.H., Li, Y., Ji, D.S., Hu, B., Kerminen,
595 V.M., Wang, Y.S., Kulmala, M.: Quantifying the impact of synoptic circulation patterns on ozone variability in northern
596 China from April to October 2013-2017, *Atmos. Chem. Phys.*, 19, 14477-14492, [https://doi.org/10.5194/acp-19-14477-](https://doi.org/10.5194/acp-19-14477-2019)
597 [2019](https://doi.org/10.5194/acp-19-14477-2019), 2019.

598 Liu, S. and Liang, X.-Z.: Observed Diurnal Cycle Climatology of Planetary Boundary Layer Height, *J. Clim.*, 23, 5790-
599 5809, <https://doi.org/10.1175/2010JCLI3552.1>, 2010.

600 Luo, R., Zheng, Y., Chen, M.: Mechanism of a rare night sudden intense warming event in Beijing and surrounding area,
601 *Meteorol. Monthly* (in Chinese), 46, 478-489, <https://doi.org/10.7519/j.issn.1000-0526.2020.04.003>, 2020.

602 Ma, Y., Yang, Y., Hu, X., Gan, R.: Characteristics and Mechanisms of the Sudden Warming Events in the Nocturnal
603 Atmospheric Boundary Layer: A Case Study Using WRF, *J. Meteorol. Res.*, 29, 747-763, [https://doi.org/10.1007/s13351-](https://doi.org/10.1007/s13351-015-4101-3)
604 [015-4101-3](https://doi.org/10.1007/s13351-015-4101-3), 2015.

605 Miltenberger, A.K., Reynolds, S., Sprenger, M.: Revisiting the latent heating contribution to foehn warming: Lagrangian
606 analysis of two foehn events over the Swiss Alps, *Q.J.R. Meteorol. Soc.*, 142, 2194-2204, <https://doi.org/10.1002/qj.2816>,
607 2016.

608 Ouyang, S., Deng, T., Liu, R., Chen, J., He, G., Leung, J.C.H., Wang, N., Liu, S.C.: Impact of a subtropical high and a
609 typhoon on a severe ozone pollution episode in the Pearl River Delta, China, *Atmos. Chem. Phys.*, 22, 10751-10767,
610 <https://doi.org/10.5194/acp-22-10751-2022>, 2022.

611 Pal, S. and Lee, T.R.: Advected Air Mass Reservoirs in the Downwind of Mountains and Their Roles in Overrunning
612 Boundary Layer Depths Over the Plains, *Geophys. Res. Lett.*, 46, 10140-10149, <https://doi.org/10.1029/2019GL083988>,
613 2019.

614 Seibert, P., Feldmann, H., Neininger, B., Bäumle, M., Trickl, T.: South foehn and ozone in the Eastern Alps – case study
615 and climatological aspects, *Atmos. Environ.*, 34, 1379-1394, [https://doi.org/10.1016/S1352-2310\(99\)00439-2](https://doi.org/10.1016/S1352-2310(99)00439-2), 2000.

616 Shu, L., Xie, M., Wang, T., Gao, D., Chen, P., Han, Y., Li, S., Zhuang, B., Li, M.: Integrated studies of a regional ozone
617 pollution synthetically affected by subtropical high and typhoon system in the Yangtze River Delta region, China, *Atmos.*
618 *Chem. Phys.*, 16, 15801-15819, <https://doi.org/10.5194/acp-16-15801-2016>, 2016.

619 Stein, A.F., Draxler, R.R., Rolph, G.D., Stunder, B.J.B., Cohen, M.D., Ngan, F.: NOAA's HYSPLIT Atmospheric Transport
620 and Dispersion Modeling System, *B. Am. Meteor. Soc.*, 96, 2059-2077, <https://doi.org/10.1175/BAMS-D-14-00110.1>,
621 2015.

622 Steinhoff, D.F., Bromwich, D.H., Speirs, J.C., McGowan, H.A., Monaghan, A.J.: Austral summer foehn winds over the

623 McMurdo dry valleys of Antarctica from Polar WRF, Q.J.R. Meteorol. Soc., 140, 1825-1837,
624 <https://doi.org/10.1002/qj.2278>, 2014.

625 Stull, R.B.: An Introduction to Boundary Layer Meteorology; Kluwer Academic Publishers, Dordrecht, The Netherlands,
626 1988.

627 Tang, G., Zhang, J., Zhu, X., Song, T., Munkel, C., Hu, B., Schäfer, K., Liu, Z., Zhang, J., Wang, L., Xin, J., Suppan, P.,
628 Wang, Y.: Mixing layer height and its implications for air pollution over Beijing, China, Atmos. Chem. Phys., 16, 2459-
629 2475, <https://doi.org/10.5194/acp-16-2459-2016>, 2016.

630 Wang, X.Y. and Wang, K.C.: Estimation of atmospheric mixing layer height from radiosonde data. Atmos. Meas. Tech. 7,
631 1701-1709, <https://doi.org/10.5194/amt-7-1701-2014>, 2014.

632 Wu, W., Fu, T.-M., Arnold, S.R., Spracklen, D.V., Zhang, A., Tao, W., Wang, X., Hou, Y., Mo, J., Chen, J., Li, Y., Feng, X.,
633 Lin, H., Huang, Z., Zheng, J., Shen, H., Zhu, L., Wang, C., Ye, J., Yang, X.: Temperature-Dependent Evaporative
634 Anthropogenic VOC Emissions Significantly Exacerbate Regional Ozone Pollution, Environ. Sci. Technol., 58, 5430-5441,
635 <https://doi.org/10.1021/acs.est.3c09122>, 2024.

636 Xu, J., Zhang, Z., Zhao, X., Zhang, J.: Synthetically impacts of the topography and typhoon periphery on the atmospheric
637 boundary layer structure and special regional pollution pattern of O₃ in North China Plain, Atmos. Environ., 330, 120566,
638 <https://doi.org/10.1016/j.atmosenv.2024.120566>, 2024.

639 Xu, X., Shu, S., Wang, G., Li, W.: Machine-learning-based identification of influencing factors and synoptic patterns of
640 foehn on the eastern foothills of the Taihang Mountains, China, Atmos. Chem. Phys., 26, 6507-6519,
641 <https://doi.org/10.5194/acp-26-6507-2026>, 2026.

642 Yang, X., Yang, M., Li, J., Zhang, S.: Impact analysis of a Taihang Mountain foehn on haze intensity, Meteorol. Monthly
643 (in Chinese), 44, 313-319, <https://doi.org/10.7519/j.issn.1000-0526.2018.02.011>, 2018.

644 Zhang, Q., Streets, D.G., Carmichael, G.R., He, K.B., Huo, H., Kannari, A., Klimont, Z., Park, I.S., Reddy, S., Fu, J.S.,
645 Chen, D., Duan, L., Lei, Y., Wang, L.T., Yao, Z.L.: Asian emissions in 2006 for the NASA INTEX-B mission, Atmos.
646 Chem. Phys., 9, 5131-5153, <https://doi.org/10.5194/acp-9-5131-2009>, 2009.

647 Zhang, S., Zeng, G., Yang, X., Wu, R., Yin, Z.: Comparison of the influence of two types of cold surge on haze dispersion
648 in eastern China, Atmos. Chem. Phys., 21, 15185-15197, <https://doi.org/10.5194/acp-21-15185-2021>, 2021.

649 Zong, L., Yang, Y., Xia, H., Yuan, J., Guo, M.: Elucidating the Impacts of Various Atmospheric Ventilation Conditions on
650 Local and Transboundary Ozone Pollution Patterns: A Case Study of Beijing, China, J. Geophys. Res.-Atmos., 128,
651 e2023JD039141, <https://doi.org/10.1029/2023JD039141>, 2023.

652

653